fractal and fractional

MDPI

Article

Influence of MgO on the Hydration and Shrinkage Behavior of Low Heat Portland Cement-Based Materials via Pore Structural and Fractal Analysis

Lei Wang [1,2,3,*], Xiao Lu [1], Lisheng Liu [2], Jie Xiao [4], Ge Zhang [1,*], Fanxing Guo [1] and Li Li [5]

[1] College of Materials Science and Engineering, Xi'an University of Architecture and Technology, Xi'an 710055, China; luxiao@xauat.edu.cn (X.L.); gfx@xauat.edu.cn (F.G.)
[2] School of Intelligent Construction, Wuchang University of Technology, Wuhan 430002, China; 120100477@wut.edu.cn
[3] State Key Laboratory of Hydrology-Water Resources and Hydraulic Engineering, Hohai University, Nanjing 210098, China
[4] School of Civil and Transportation Engineering, Guangdong University of Technology, Guangzhou 510006, China; xiaojie2017@gdut.edu.cn
[5] College of Water Resources and Architectural Engineering, Northwest A&F University, Xianyang 712100, China; drlili@nwafu.edu.cn
* Correspondence: wanglei535250684@xauat.edu.cn (L.W.); zhangge@xauat.edu.cn (G.Z.)

Abstract: Currently, low heat Portland (LHP) cement is widely used in mass concrete structures. The magnesia expansion agent (MgO) can be adopted to reduce the shrinkage of conventional Portland cement-based materials, but very few studies can be found that investigate the influence of MgO on the properties of LHP cement-based materials. In this study, the influences of two types of MgO on the hydration, as well as the shrinkage behavior of LHP cement-based materials, were studied via pore structural and fractal analysis. The results indicate: (1) The addition of reactive MgO (with a reactivity of 50 s and shortened as M50 thereafter) not only extends the induction stage of LHP cement by about 1–2 h, but also slightly increases the hydration heat. In contrast, the addition of weak reactive MgO (with a reactivity of 300 s and shortened as M300 thereafter) could not prolong the induction stage of LHP cement. (2) The addition of 4–8 wt.% MgO (by weight of binder) lowers the mechanical property of LHP concrete. Higher dosages of MgO and stronger reactivity lead to a larger reduction in mechanical properties at all of the hydration times studied. M300 favors the strength improvement of LHP concrete at later ages. (3) M50 effectively compensates the shrinkage of LHP concrete at a much earlier time than M300, whereas M300 compensates the long-term shrinkage more effectively than M50. Thus, M300 with an optimal dosage of 8 wt.% is suggested to be applied in mass LHP concrete structures. (4) The addition of M50 obviously refines the pore structures of LHP concrete at 7 days, whereas M300 starts to refine the pore structure at around 60 days. At 360 days, the concretes containing M300 exhibits much finer pore structures than those containing M50. (5) Fractal dimension is closely correlated with the pore structure of LHP concrete. Both pore structure and fractal dimension exhibit weak (or no) correlations with shrinkage of LHP concrete.

Keywords: low heat Portland cement; MgO; hydration; strength; shrinkage; pore; fractal dimension

Citation: Wang, L.; Lu, X.; Liu, L.; Xiao, J.; Zhang, G.; Guo, F.; Li, L. Influence of MgO on the Hydration and Shrinkage Behavior of Low Heat Portland Cement-Based Materials via Pore Structural and Fractal Analysis. *Fractal Fract.* **2022**, *6*, 40. https://doi.org/10.3390/fractalfract6010040

Academic Editor: Zine El Abiddine Fellah

Received: 13 December 2021
Accepted: 9 January 2022
Published: 12 January 2022

1. Introduction

Low heat Portland (LHP) cement or high-belite cement is featured by a significantly larger proportion of belite (C_2S) and a smaller proportion of alite (C_3S) compared with conventional ordinary Portland cement (or ASTM Type I and CEM I) [1,2]. Due to the much slower hydration rate and higher content of C_2S than C_3S in LHP cement, the hydration heat generated by LHP cement is much lower than OPC [3–6]. For example, the accumulated hydration heat of LHP cement at 3, 28, and 360 days is about 15.6–25.0%, 14.9–18.0%, and 15.3% lower than that of OPC, respectively [3,5–7]. Similarly, given the same proportions,

the peak adiabatic temperature of LHP cement concrete is about 5.5–6.2 °C lower than OPC concrete [3,5,6]. The conditions in mass concrete are nearly adiabatic and the peak temperature can easily achieve as high as 50–80 °C, and the large temperature difference between inside and outside of structures can easily lead to thermal stress development and cracking [8]. Therefore, LHP cement is a perfect cement to be used in mass concrete structures, which could obviously reduce the potential thermal-stress-induced cracking risk [1,4]. In recent years, LHP cement was utilized in dozens of huge dams in China to replace OPC, e.g., Baihetan dam, Wudongde dam, etc. [3,6,9]. However, the thermal stress of LHP cement-based materials cannot be considerably avoided since the hydration of LHP cement still releases a large amount of heat, even though its peak value is declined and postponed to some extent compared with OPC. Moreover, the LHP cement concrete would inevitably shrink due to the chemical reaction of cement and moisture loss in the drying environment, which also increase the cracking risk [6,10]. Therefore, how to reduce the shrinkage of LHP cement concrete remains a challenging issue for engineers.

Generally, several strategies are utilized to control temperature and prevent cracks in practical engineering, including the adoption of pre-cooling aggregate and ice water, a pipe cooling method by circulating cold water through internal pipes during the concrete hardening stage [11], and the usage of a certain dosage of fly ash [12–15], fibers [16–23], and a magnesia expansion agent (abbreviated as MgO thereafter) [24–30]. However, the pre-cooling method and pipe cooling method need some additional labor as well as more construction time and cost [11]. Moreover, the presence of fly ash would decrease the mechanical strength of LHP concrete at early age and therefore prolong the construction period [10].

MgO, which is manufactured by calcining magnesite or any other magnesium ore, is reported to be used in mass concrete of dozens of dams in the past few decades to minimize or eliminate the expensive temperature control measures in dam construction [27,31]. This is because the reaction of MgO tends to produce a certain volume expansion that could compensate part of or all of the shrinkage of concrete [25–28], which could consequently lower the cracking risks of structure [24–29]. According to Chinese standard DL/T 5296-2013 [32], there are two types of MgO, namely a reactive type with a neutralization time between 50 to 200 s (i.e., Type I MgO) and a weak reactive type with a neutralization time ranging from 200 to 300 s (i.e., Type II MgO). Many studies have reported that Type I MgO could produce quicker expansion at an early age than Type II MgO. Thus, it was more applicable for compensating the early quick shrinkage of thin concrete structures resulting from the rapid loss of water from their highly exposed surfaces or from a rapid temperature drop at initial hydration time when the concrete tensile strength is not high [25,33,34]. On the contrary, Type II MgO, which begins to produce expansion only at a later age, is more beneficial for massive concrete structures, since it can compensate the thermal stress-induced shrinkage that persists for one or more years after concrete casting [28,33,35,36].

Although there are extensive studies thus far regarding the influence of MgO on shrinkage properties and pore structures of conventional Portland cement pastes, mortars, and concretes, very little work has been carried out on the effects of MgO on micro- or macro-properties of LHP cement-based materials. Due to the extensive usage of LHP cement in hydraulic projects and civil engineering in China, as well as the urgent need to further reduce the cracking risk of LHP concrete structures, a comprehensive investigation of the influence of MgO with different reactivity on properties of LHP cement-based materials is required. Herein, the influence of two types of MgO on LHP cement hydration, mechanical properties, and shrinkage behavior of LHP concrete were comprehensively studied and accessed. Moreover, the effects of MgO were analyzed in terms of pore structure and fractal theory. The findings in this work help to use MgO properly in designing LHPconcrete with low shrinkage and cracking risk.

2. Materials and Analytical Methods

2.1. Materials

LHP cement with a 42.5 grade was provided by HuaXin Cement Plant, China, and MgO expansive agent with two reactivities, namely 50 s and 300 s were used. The reactivity of MgO was tested conforming to Chinese Standards [32,37]. These MgO were manufactured by calcining magnesite at 900 °C and 1100 °C, respectively, and provided by Sanyuan New Materials Co., Ltd. The two types of MgO, which are shortened as M50 and M300 thereafter, meet the standard requirements for Type I MgO and Type II MgO, respectively, based on DL/T 5296-2013 [32]. The mineral compositions of LHP cement, which were provided by HuaXin Cement Plant, are 28.7 wt.% C_3S, 47.0 wt.% C_2S, 4.1 wt.% C_3A, 12.8 wt.% C_4AF, and 3.9 wt.% gypsum. LHP cement meets the technical requirements for type IV Portland cement (low heat cement) conforming to ASTM C150 [38] and LHP cement conforming to GB 200 [39]. The basic physical properties and chemical oxides of LHP cement and MgO are exhibited in Table 1.

Table 1. Physical property, chemical oxides of LHP cement, and MgO.

Parameter	LHP Cement	M50	M300
Oxides (wt.%)			
CaO	61.9	2.4	2.6
SiO_2	23.9	1.3	1.4
Fe_2O_3	4.2	0.6	0.5
MgO	2.9	91.2	91.0
SO_3	2.3	0.1	0.1
Al_2O_3	4.2	0.1	0.1
Loss on ignition	0.5	3.7	3.1
Physical property			
Specific surface area (SSA) by Blaine (m^2/kg)	318	-	-
SSA by BET (m^2/g)	0.86	31.2	12.50
Median particle size (D50, μm)	17.6	11.8	19.8
Specific gravity	3.22	3.51	3.50

Coarse aggregate and fine aggregate are made of crushed limestone. The maximal particle size of coarse aggregate and fine aggregate are 40 mm and 5 mm, respectively. The density for both coarse and fine aggregates is 2650 kg/m^3. The fineness modulus of fine aggregate is 2.71.

2.2. Mix Proportion Design

The proportions of cement paste prepared were showed in Table 2. The cement pastes in this study were used for hydration heat tests. Three MgO dosages (0, 4 wt.%, and 8 wt.% by mass of binder) were used to prepare the paste samples. In Table 2, the LHP cement pastes added with 4 wt.% and 8 wt.% Type I MgO are labelled as "LP0", "LP4M50", and "LP8M50". Similarly, pastes with 4 wt.% and 8 wt.% Type II MgO were named "LP4M300" and "LP8M300", respectively.

Table 2. Mixture proportion of paste samples.

Designations	Water to Binder Ratio	MgO Content (wt.%)
LP0	0.28	0
LP4M50	0.28	4
LP8M50	0.28	8
LP4M300	0.28	4
LP8M300	0.28	8

The concrete specimens were used to study the effects of MgO on mechanical property, drying, and autogenous shrinkage, pore structures, and fractal characteristics of LHP

concrete. In practical applications, a MgO dosage range of 4–8% is usually suggested [36]. Thus, the MgO replacement for cement ratios of 0, 4 wt.%, and 8 wt.% were adopted to prepare the concrete. By using a polycarboxylate-based water reducing agent, a target concrete slump value around 60 mm can be obtained. Table 3 shows the concrete mixture proportions of concrete. For example, the LHP concrete sample without MgO is assigned as the control sample and labeled "LC0", the sample added with 4 wt.% M50 is labelled "LC4M50", and the sample with 8 wt.% Type II MgO is named "LC8M300".

Table 3. Mixture proportion of concrete.

Designations	W/B Ratio	MgO Dosage (wt.%)	Mix Proportions (kg/m^3)						Slump (mm)
			Water	Cement	MgO	Sand	Coarse Aggregate	Water Reducing Agent	
LC0	0.4	0	125	313	0	626	1330	2.2	65
LC4M50	0.4	4	125	300	13	626	1330	2.8	55
LC8M50	0.4	8	125	288	25	626	1331	3.1	51
LC4M300	0.4	4	125	300	13	626	1330	2.5	62
LC8M300	0.4	8	125	288	25	626	1331	2.8	57

All of the LHP concrete and paste samples were kept in a standard curing chamber until tested.

2.3. Test Methods

2.3.1. Hydration Heat Tests by TAM AIR

As described above, hydration heat of cement is important in determining the thermal stress and cracking risk of concrete. In this work, the 3-day hydration heat was tested by using a TAM AIR (TA Instruments, New Castle, DE, USA) calorimeter complying with ASTM C1702 [40]. When testing, about 6 g of fresh paste was put in a sealed glass tube immediately after mixing the binder with water, then the hydration heat was tested by the calorimeter every 1 min for up to 3 days. Three paste samples for each paste mixture shown in Table 2 were tested at the same time and the average result was reported as a hydration heat result.

2.3.2. Mechanical Properties

Compressive and splitting tensile strength are important mechanical properties of concrete [41–44]. Concrete mechanical properties in this work were determined on the cubic specimens sized 150 mm × 150 mm × 150 mm according to DL/T 5150 [45]. Six and three specimens were tested for a compressive strength and a splitting tensile strength, respectively for each mixture, and the mean value was reported.

2.3.3. Shrinkage Behavior

The shrinkage of concrete mainly includes the autogenous shrinkage and drying shrinkage, both of which are the primary reasons of cracking in concrete structures [46–48]. The drying shrinkage of concrete results from the free moisture loss from the internal pores in a drying environment [6]. The autogenous shrinkage is generated by the cement hydration that consumes the capillary water and consequently produces high capillary tension [49].

As for the autogenous shrinkage tests conforming to DL/T 5150 [45], the barrels made of galvanized sheet with a size of Φ 200 mm × 500 mm were prepared, and then one resistance strainometer was fixed in each barrel. The concrete was cast put into the barrel. Then, the barrels were soldered and stored in a chamber maintained at about 20 °C. For each mixture, two specimens were prepared and tested. During the tests, the data

were recorded continuously up to 360 days. The description of the detailed calculation of autogenous shrinkage can be seen in previous studies [6,50].

As for the drying shrinkage tests complying with DL/T 5150 [45], the concrete samples sized 100 mm × 100 mm × 515 mm were prepared. At first, the initial length of the prisms was recorded, then the prisms were maintained in a drying chamber with a temperature of about 20 °C and an RH of about 50%. The length of prisms were recorded for 360 days. Three prisms for each concrete mixture were tested and the mean drying shrinkage result was reported.

2.3.4. Pore Structural Tests by Mercury Intrusion Porosimeter (MIP)

Most macro properties of concrete including mechanical property and shrinkage behavior are considered to be related with pore structure [51–53]. The porosity and pore size distribution are the main pore structure parameters [50,54,55]. MIP is widely employed to analyze the pore structure parameters of porous materials [50,55,56]. In this study, the pore structure parameters of LHP concrete were measured by MIP. This MIP instrument is a AutoPore IV 9500 model. The cubic samples sized around 5–8 mm were cut from the concrete samples used for strength test. The coarse aggregates should be removed from the cubic samples before the MIP test.

2.3.5. Fractal Dimension Calculation

The pore structures of concrete are complex, which are be investigated in terms of fractal theory [15,51,55,57–66]. Fractal theory is a new method of mathematics, resolving the irregularities in nature [67–70]. Many researchers [71–78] demonstrated that fractal theory links microstructures with the macro-performance of cement-based materials well, and vice versa.

Some fractal models on the basis of MIP results such as Zhang's model [79,80] and Neimark's model [56] can be employed to study the fractal characteristics of concrete. According to Pfeifer and Avnir [81], the fractal dimension of pore surface fractal dimension (D_s) reflects the roughness and irregularities of pore surfaces of porous material. D_s can be obtained from Zhang's model.

According to Zhang's fractal model [79,80], during the MIP experiment, the correlation between accumulated injection work (W_n) on mercury and the total volume mercury injected into the pores (V_n) obeys a logarithmic relationship, which can be expressed as Equation (1):

$$ln\frac{W_n}{r_n^2} = D_s ln\frac{V_n^{1/3}}{r_n} + C \quad (1)$$

where r_n is the pore radius m; C is a regression constant; n means the n-th mercury injection.

W_n can be calculated by the following Equation (2):

$$W_n = \sum_i^n p_i \triangle V_i \quad (2)$$

where the index i is the i-th mercury injection; p_i refers to as the mercury pressure Pa; V_i denotes the volume of mercury injected at the i-th injection, m^3.

At first, the values of W_n, V_n, $ln\frac{W_n}{r_n^2}$, and $ln\frac{V_n^{1/3}}{r_n}$ can be determined on the basis of MIP results and Equation (2). Then, D_s can be calculated, which is the slope of the straight line in Equation (1).

3. Results and Discussion

3.1. Hydration Heat Results of LHP Cement Paste Added with MgO

The hydration heat results of LHP cement added with MgO (LP0, LP4M50, LP8M50, LP8M300, and LP8M300) are shown in Figure 1.

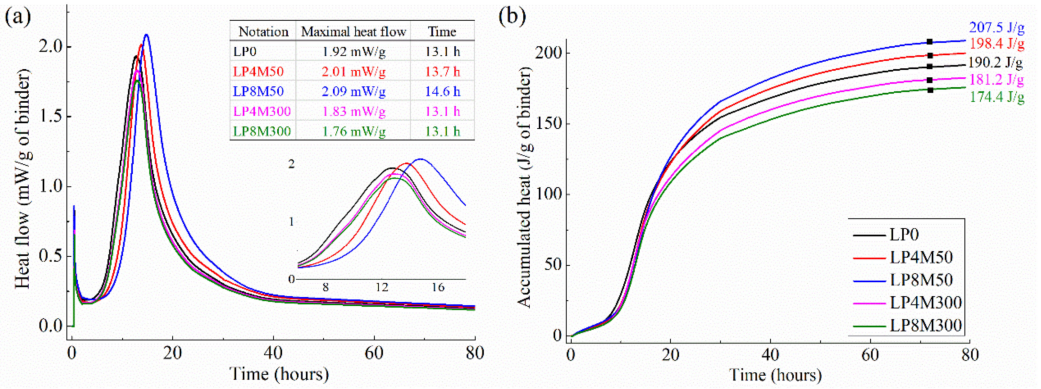

Figure 1. The 3-day hydration heat: (**a**) heat flow and (**b**) the accumulated hydration heat.

Figure 1a exhibits that all of the pastes exhibit five stages of hydration heat evolution, that is, the first exothermic peak appears within the first 0–2 h of hydration, thereafter an induction stage that may last about 2 to 4 h can be found, then the second exothermic peak appears in the acceleration stage. After that the hydration rate slows down steadily with hydration age until it reaches a relatively constant value. From Figure 1, it can be also seen that the effects of MgO on hydration kinetics of LHP cement depend on the reactivity and content of MgO.

The addition of M50 not only prolongs the induction stage of LHP cement for about 1–2 h but also increases the hydration heat slightly, and these effects would enhance as the dosage of M50 increases from 4% to 8%. On the one hand, Figure 1a displays the induction stage of LP4M50 and LP8M50 is slightly prolonged by 1–2 h compared with LP0. The occurrence of the second exothermic peak of LP4M50 and LP8M50 is postponed by about 0.6 and 1.5 h, respectively, compared with LP0. These phenomena were also observed by Kabir and Hooton [28], who found the second exothermic peak of OPC was 1–1.5 h delayed by the replacement of 10 % of 55 s MgO powders. A similar finding was reported by Zheng et al. [82] who found the addition of 4% MgO delays the occurrence of the second exothermic peak by about 1.2 h and this retarding effect is more prominent with increasing MgO dosage. They elaborated two main mechanisms responsible for this retarding phenomenon [82]: (1) due to the rapid crystallization and precipitation of $Mg(OH)_2$ (also termed as brucite) from cement paste solution that reduces the concentration of OH^- ions, the time when the $Ca(OH)_2$ saturation ratio reaches the maximum is increased, and thus, the initiation of the second peak on the heat evolution curve of cement, i.e., the end of the induction period, is delayed; (2) the generated brucite with a tiny crystallite size could precipitate on the cement grain surfaces to form a thin layer which retards further hydration of the cements.

On the other hand, Figure 1a clearly demonstrates that LP4M50 and LP8M50 present higher maximal heat flows and accumulated hydration heat than LP0. For instance, the accumulated 3-day hydration heat of the LP one is 190.2 J/g of binder, while those of LP4M50 and LP8M50 pastes are 198.4 and 207.5 J/g, inceased by 4.3% and 9.1%, respectively. It should be noted that this increase in hydration heat is not controversial to the retarding discussed above, because the retarding effect occurs in the induction stage while the increase in the hydration heat appears in the acceleration stage. In fact, other researchers also reported the similar findings. Zheng et al. [82] found that OPC added with 4% MgO exhibits 7 J /g (about 4%) higher hydration heat than the plain OPC paste within 2 days. They attributed this phenomenon to the rapid heat evolution of reactive MgO at early hydration time. As evidenced by other researchers, the total accumulated hydration heat for a completely hydrated MgO is 800 J/g [83] or 930 J/g [84], which is much larger than that of OPC, which is commonly around 200 J/g [82]. Moreover, it was confirmed that the reactive MgO (46 s) could react with water when it is mixed with water and achieve a hydration degree about 97% at 2 days [85]. What is more, reactive MgO usually exhibits the peak value of hydration heat flow at about 10 h, which is very close to the second

exothermic peak of cement and inevitably produces a superposition of heat flow peak with cements [83,84]. Due to the reasons mentioned above, the second exothermic peak value of cement in Figure 1 is strengthened and total hydration heat is increased in the presence of M50.

On the contrary, the addition of M300 could neither prolong the induction stage of LHP cement or increase its hydration heat. Specifically, Figure 1a shows that, the end time of induction period and the occurrence time of the maximal heat flow of LP4M300 and LP8M300 are almost the same with that of the LP one, but the maximal heat flow value is reduced by some degrees. Moreover, Figure 1b shows that the accumulated hydration heat of LP4M300 and LP8M300 are about 4.7% and 8.3% lower than that of the LP one, respectively. The reduced hydration heat is proportional to the dosage of M300. These results indicate that M300 seems to act as an inert material at the early stage of cement hydration. This trend has also been reported by other studies [36,85]. Mo et al. [85] reported that the hydration degree of M300 with water is only 4.5% at 2 days and 9.9% at 7 days. Thus, the reduced amount of cement due to the dilution effect of M300 is the main reason for the reductions in both the maximal heat flow and accumulated hydration heat.

3.2. Mechanical Property of LHP Concrete Added with MgO

The mechanical properties of LHP concrete containing MgO are shown in Figure 2. The error ranges of these strength results are also exhibited in Figure 2. Figure 2 clearly illustrates that the MgO reactivity and content have great influences on mechanical property of LHP concrete.

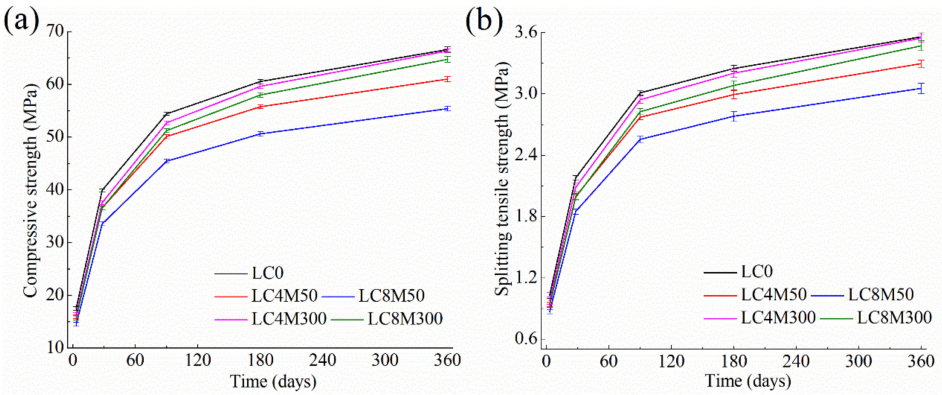

Figure 2. Mechanical property of LHP concrete containing MgO: (**a**) compressive strength and (**b**) splitting tensile strength.

Concerning the MgO dosage, Figure 2 shows that both the compressive strength and splitting tensile strength of concrete are reduced in the presence of MgO. A higher MgO dosage leads to a larger strength reduction, regardless of MgO reactivity. For example, the addition of 4% M50 and M300 lowers the compressive strength by 8.9% and 6.5% at 3 days, 8.4% and 5.9% at 28 days, and 8.4% and 0.4% at 360 days, whereas the reductions due to addition of 8% M50 and M300 are 16.9% and 10.1% at 3 days, 16.0% and 8.4% at 28 days, and 16.8% and 2.8% at 360 days. The strength reduction resulting from MgO addition has been reported elsewhere [86,87]. The following reasons can explain this reduction: (1) The reduced cement content would inevitably lead to less hydration products especially C-S-H, which dominates the strength of cement-based materials [87–90]. (2) The formation of brucite contributes little to the strength development of cement pastes or concrete, since brucite exhibits no binding properties alike C-S-H [84,91]. Thus, although M50 could react with water fully at early age, the generated brucite crystals is not helpful for the strength gain of concrete. (3) Other possible reasons have also been reported to result in weakened strength of concrete, such as the additional water consumption by MgO reaction [87] and increased micro-cracks and porosity caused by brucite formation and growth [88,92].

Regarding the effects of MgO reactivity, Figure 2 shows that in comparison with M300, the addition of more reactive M50 tends to reduce the mechanical property of LHP concrete to a greater extent at all periods studied. The compressive strength of LC8M300 at 3, 28, 180, and 360 days was 10.1%, 8.4%, 4.2%, and 2.8% lower, respectively, as compared to the LC0 one, while the compressive strength of LC8M50 at 3, 28, 180, and 360 days was 16.9%, 16.0%, 16.4%, and 16.8% lower than those of LC0. The same trend can be found for LC4M300 and LC4M50 and for the splitting tensile strengths in Figure 2 as well the results in other study [91]. Cao et al. [91] reported that the more reactive the MgO is, the larger the strength reduction of concrete is. Thus, it can be deduced that the replacement of cement by MgO is the main reason for the strength reduction of concrete containing M300, since M300 cannot participate the reaction at early age. As Mo et al. [85] showed, the 7-day reaction degrees of less reactive MgO (325 s) and reactive MgO (46 s) are about 10% and 100%, respectively. Apart from the replacement of cement, M50 could consume more free water and react with water considerably at an early age, resulting in larger strength reductions.

Moreover, the results in Figure 2 indicate that the addition of M300 favors the strength development of LHP concrete at late age, while M50 is not helpful for the long-term strength. Specifically, LC4M300 and LC8M300 exhibit almost the same 180-day and 360-day compressive and splitting tensile strengths with LC0 concrete, whereas LC4M50 presents 7.2–8.4% lower and LC8M5 presents 14.2–16.7% lower 360-day strength than the LC0 concrete. This is consistent with the results reported by Choi et al. [93], who found that the compressive strength of concrete added with 5% MgO (265 s) began to increase after the hydration time of 56 days and achieved a comparable strength with the control at 180 days. They attributed this long-term strength increment to the expansion caused by less reactive MgO that could react with water and densify the microstructure of concrete at late age. The same finding has also reported by Cao et al. [91]. They pointed that that weak reactive MgO at middle and long-term age could react and dense the pore structures, thus reducing the strength gap between MgO concrete and control sample. In contrast, MgO with high reactivity reacts with water quickly and completely at early age, but could lower the early strength of concrete and contribute little to the late-age strength.

3.3. Autogenous Shrinkage

The autogenous shrinkage of LHP concrete containing MgO are shown in Figure 3.

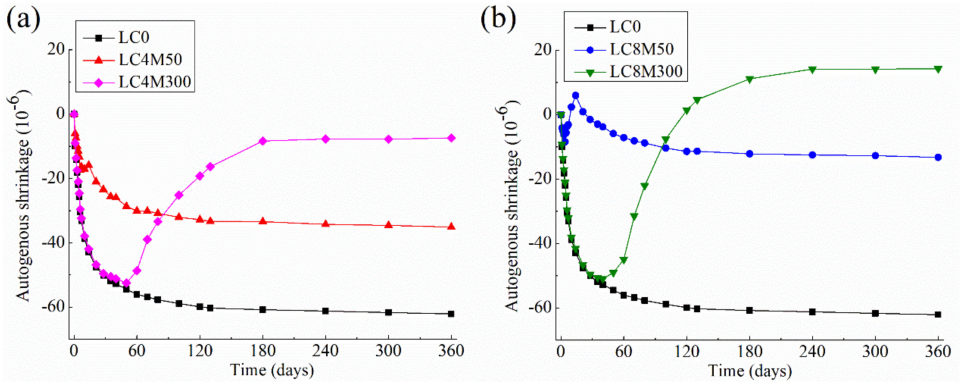

Figure 3. Autogenous shrinkage of LHP concrete containing two kinds of MgO at a dosage of (**a**) 4% and (**b**) 8%.

It can be observed from Figure 3 that the autogenous shrinkage of LHP concrete has been significantly reduced by the addition of MgO.

Regarding the influence of MgO reactivity, Figure 3 indicates that both M50 and Mg300 can compensate the autogenous shrinkage of LHP concrete, but they differ in the occurrence time and the duration of compensation effect. Specifically, LC4M50 and LC8M50 start to shrink during the first few days until they reach the first inflexion points at about 5 days. The first inflexion point occurs when the expansion due to MgO hydration exceeds the

value of autogenous shrinkage due to cement hydration. The similar inflexion points due to MgO hydration have been also reported by others [36,87,94]. About 12.4 $\times$ 10^{-6} and 20.1 $\times$ 10^{-6} of autogenous shrinkage of LC4M50 and LC8M50 can be compensated at 5 days, respectively. After the first inflexion points, they begin to climb up to the second inflexion points at about 14 days, when M50 exhibits the maximal shrinkage-compensating effect. Thereafter, they start to shrink significantly and reach a constant value between 180 and 360 days. From the trend revealed above, it can be seen that although M50 can effectively compensate the shrinkage at early age, it exhibits much little or even no compensation action afterwards until the age of 360 days. This finding corresponds well with the autogenous shrinkage results of cement pastes [87] and mortars containing MgO with various reactivities [33].

In addition, Figure 3 clearly shows the first inflexion points of LC4M300 and LC8M300 occur at about 50 days, which is much later compared with those of LC4M50 and LC8M50. This is because the weak reactive M300 begins to react with water at middle age, as discussed above. After the first inflexion points, the autogenous shrinkage curves of LC4M300 and LC8M300 start to climb up until the hydration age of 180 days when they reach a relatively constant value. It can be seen that there is a very long duration of compensation effect for M300. From then on, the curves of LC4M300 and LC8M300 stay rather flat between 180 days and 360 days. At 360 days, about 88% and all of the autogenous shrinkage can be eliminated resulting from the addition of 4% and 8% M300, respectively. These results are similar to those found by Mo et al. [85], who reported that more time is needed for the expansion curve to become flat when the MgO reactivity is weak. Moreover, LC4M300 and LC8M300 do not show the second inflexion points in their autogenous shrinkage curves. This is because even though the compensation effect of M300 disappears at long-term hydration age, the shrinkage caused by cement hydration is small at the same time; as a result the concrete would not exhibit obvious shrinking trend at late age.

Figure 3 also shows that increasing MgO content from 0 to 8% could enhance the compensation effect of both M50 and M300. For instance, a nearly 43.5% reduction in autogenous shrinkage of LC0 at 360 days can be found after the addition of 4% M50, while this reduction is 78.7% due to the addition of 8% M50. It should be noted here that the usage of 8% M50 cound not compensate for the autogenous shrinkage of LC0 completely, but this can be done by adding 8% M300. The addition of 4% M300 produces a final autogenous shrinkage strain of -7.4×10^{-6}, while adding 8% M300 produces a 360-day expansion of 14.3 $\times$ 10^{-6}. Overall, this enhanced compensation effect with MgO dosage is in good aggreement with the results obtained from cement pastes [25,87,94], mortars [34,89], and concretes [27,31,95].

3.4. Drying Shrinkage

The drying of LHP concrete containing MgO are shown in Figure 4.

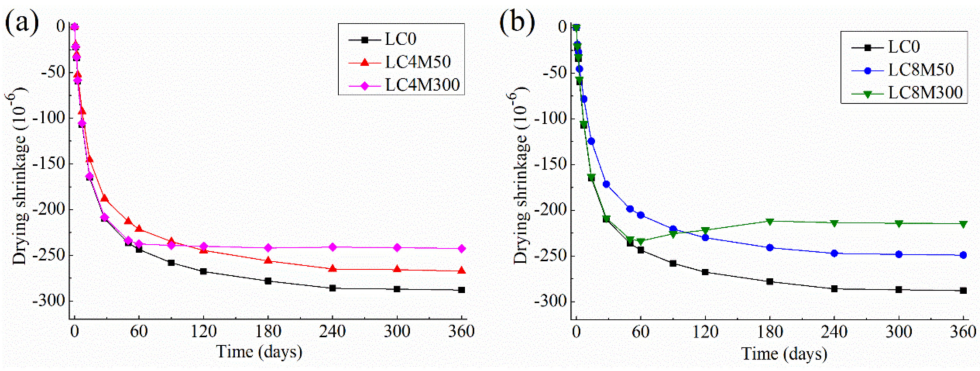

Figure 4. Drying shrinkage of LHP concrete containing two kinds of MgO at a dosage of (**a**) 4% and (**b**) 8%.

Figure 4 shows that the majority of drying shrinkage of control LHP concrete (LC0) occurs during the first 2–3 weeks of hydration. Additionally, Figure 4 displays that the addition of MgO with different kinds and content affects drying shrinkage significantly.

Regarding the MgO reactivity, Figure 4 shows that M50 compensates the drying shrinkage of LHP concrete at much earlier age than M300, but produces a much weaker and shorter duration of compensation effect. Specifically, M50 begins to reduce the drying shrinkage of LHP concrete at the very initial hydration time of 1–2 days, whereas M300 starts to eliminate the drying shrinkage during 60–90 days of hydration. About 10.9% and 21.0% of drying shrinkage of LC0 at 2 days can be reduced by adding 4% and 8% dosage of M50, respectively. This finding is in good agreement with the autogenous shrinkage results in this work, as well as the results of cement paste obtained by Mo et al. [85], who pointed out that as soon as the reactive MgO (47 s) mixed with water it begins to react and produces a large volume expansion whereas the less reactive MgO (325 s) starts to compensate the drying shrinkage of cement paste at much later age.

The results in Figure 4 also show that M50 achieves its maximum compensation effect (i.e., the largest expansion due to MgO hydration) between 10–14 days, when approximately 12.0% (19.7×10^{-6}) and 24.6% (40.6×10^{-6}) of drying shrinkage of LC0 concrete could be reduced after the addition of 4 % and 8 % M50, respectively. Afterwards, no more drying shrinkage can be compensated by M50, both LC4M50 and LC8M50 present quite similar shrinking behavior to the LC0 until 360 days, when the drying shrinkage of LC4M50 and LC8M50 are 7.2% and 13.5% lower than that of LC0, respectively. In contrast, Figure 4b indicates that the shrinkage curve of LC8M300 steadily climb up until 180 days, indicating M300 exhibits a much longer duration of compensation effect than M50. Thereafter LC8M300 maintains a nearly constant shrinkage value until 360 days. Finally, about 16.0% and 25.5% of the 360-day drying shrinkage is reduced by adding 4% and 8% M300, respectively. Similar compensation effects of MgO have been observed on cement mortars reported by Cao et al. [33,34,91].

Regarding the MgO dosage, it could be observed from Figure 4 that the increase in MgO content from 0 to 8% enhanced the compensation effect on drying shrinkage. For instance, the addition of 4% of M50 and M300 eliminates the 360-day drying shrinkage of LC0 concrete by 7.2% and 13.5%, respectively, while the 8 % addition of M50 and M300 compensates about 16.0 % and 25.5% drying shrinkage of LC0 at 360 days, respectively. This is because larger dosage of MgO would produce a larger amount of brucite and thus yield greater expansion [25,95]. Moreover, it is noticeable that even the addition of 8 % M300 could compensate only 25.5% of the total drying shrinkage of LC0 concrete, that is to say, LC8M300 still exhibits a rather obvious shrinking behavior. Kabir and Hooton [28] have reported the similar findings; they found that the drying shrinkage values of both cement paste and concrete containing MgO with two reactivities of 55 s and 210 s are rather large at a high MgO dosage of 15%. This is because the expansion caused by M300 hydration in this study is much smaller than the shrinkage of concrete caused by drying.

In summary, M50 compensates the shrinkage of LHP concrete at much earlier hydration age than M300; however, this compensation effect cannot last long and is not as efficient as M300. In contrast, M300 is nearly inert at early age but could compensate the long-term shrinkage more effectively than M50. Considering the fact that LHP cement is mostly used in mass concrete whose thermal cracking risk is high at long-twem age [28,33,35,36], MgO with weak reactivity and high content is suggested to be adopted in mass LHP concrete structures. Nevertheless, the dosage of MgO should be less than 8%, since a higher dosage may cause significant loss in early mechanical properties of concrete, as demonstrated in Section 3.2, or lead to harmful expansion that may cause soundness problems, as reported by Cao et al. [91].

3.5. MIP Results

The pore structure parameters of LHP concrete containing MgO at 7, 60 and 360 days, which denote the early age, middle age, and long-term age, respectively, are given in Table 4.

Based on the classification method [96], pores with the size range of 2.5–10 nm, 10–50 nm, and 50–10 μm, should be ascribed to small gel pores, medium capillary pores, and large capillary pores, respectively. Table 4 shows that, as hydration proceeds, the proportion of large capillary pores in LC0 concrete increases continuously while the proportions of medium and small capillary pores as well as the porosity decrease. This is because the pores could be filled up by hydration products during hydration [12,50]. Moreover, Table 4 indicates the MgO with different reactivities and dosages has an appreciable influence on pore structure of LHP concrete.

Table 4. Pore structure parameters of concrete obtained by MIP.

Designations	Hydration Age (Days)	The Most Probable Pore Diameter (nm)	Porosity (%)	Pore Size Distribution		
				<10 nm (%)	10–50 nm (%)	50 nm–10 μm (%)
LC0	7	155	35.2	7.3	24.6	67.4
	60	72.5	24.1	14.7	46.5	38.5
	360	32.6	15.6	22.2	59.3	17.6
LC4M50	7	121.3	31	7.9	33.2	58.2
	60	58.7	20.2	14.8	49.3	35.5
	360	28.2	13.2	22.5	61.2	15.3
LC4M300	7	157.4	35.8	6.9	22.9	69.8
	60	65.2	22.3	13.5	49.8	36.4
	360	21.5	11.6	22.6	64.1	12.9
LC8M50	7	102.2	26.5	7.1	39.1	52.9
	60	42.5	18.7	13.5	53.2	31.6
	360	25.7	11.5	21.8	63.3	13.6
LC8M300	7	160	36.3	6.5	21.4	71.3
	60	60.2	20.9	12.1	53.2	34.3
	360	18.3	8.9	22.0	67.3	10.3

Regarding the influence of MgO reactivity, Table 4 illustrates that the addition of M50 obviously reduces the porosity, the most probable pore diameter and the fraction of large capillary pores (between 50 nm and 10 μm) at 7 days. On the contrary, the addition of M300 could not change the pore structure parameters of LHP concrete at 7 days. This is similar with other MIP study [86], in which cement paste added with 8% reactive MgO (45 s) exhibits much lower porosity than the plain cement pastes at early age, whereas those containing 8% less reactive MgO (135 s) exhibit the similar pore structure parameters with the control at the same time. There are two possible reasons to explain this result. First, the reactive MgO can rapidly react with water to produce large amount of brucite to fill up the pores at early age while the weak MgO cannot. This is evidenced by a thermal analysis [25], which demonstrates that the content of brucite formed in the cement pastes added with weak reactive MgO is less than that formed in the pastes containing reactive MgO (45 s). Secondly, the generated brucite could produce some expansion, which could further reduce the porosity and lower the large pore proportions. It was suggested that the expansion caused by brucite tends to densify the pore structure of cement pastes [25] and concretes [13].

In contrast, Table 4 illustrates that M300 begins to refine the pore structure of LHP concrete at 60 days. At 360 days, the LHP concretes containing M300 exhibit much finer pore structure than those containing M50 and LC0. For instance, LC4M300 cured at 360 days has a porosity of 11.6%, the most probable pore diameter of 21.5 nm and the proportion of large capillary pores of 12.9%, all of which are smaller than those of LC4M50 (13.2%, 28.2 nm, and 15.3%, respectively). The similar results can be found from an MIP study for mortar [93], in which the porosity and proportion of large pores of mortars containing 5 % MgO with a weak reactivity of 265 s were much lower than those of plain cement mortar at 360 days. They attributed these phenomena to the facts that the weak reactive MgO could produce products at late age which could fill the pores and transform large pores into small ones [93].

Moreover, it should be noted that the addition of MgO would not noticeably change the proportions of small capillary (gel) pores during the whole hydration process, regardless of the reactivity of MgO. This is because the proportions of capillary (gel) pores are related with the quantities of gel, such as C-S-H and other gel phases [6], while the reaction of MgO produces solely the crystalline phase brucite and could not increase the gel quantity at all.

Regarding the influence of MgO dosage, Table 3 indicates that increasing MgO dosage from 4% to 8% reduces the porosity and proportion of large capillary pore significantly. In other words, the refinement of the pore structures enhances with increasing MgO dosage. For instance, LC8M50 cured at 7 days exhibits a porosity of 26.5%, the most probable pore diameter of 102.2 nm and the proportion of large capillary pores of 52.9%, all of which are smaller than those of LC4M50 at the same time, which are 31.0%, 121.3 nm, and 58.2%, respectively. The similar trend can be observed for LC4M300 and LC8M300. This trend could be attributed to the stronger densification effect of MgO at higher dosage level, that is, the higher dosage of MgO can produce more brucite to fill the pores, resulting in a lower porosity and smaller proportion of large capillary pore, i.e., a denser pore structure.

3.6. Fractal Dimension of Pore Surface (D_s)

The Fractal dimension of pore surface (D_s) of control LHP concrete (LC0) and concretes containing MgO with different reactivities and dosages at 7, 60, and 360 days are shown in Table 5. The correlation coefficients (R^2) of the fitting line in Equation (1) was also listed in Table 5, which are so close to 1.0, demonstrating the obtained D_s values are accurate and reliable.

Table 5. Pore surface fractal dimension of LHP concrete added with MgO.

Designations	Hydration Age (Days)	D_s	R^2
LC0	7	2.721	0.953
	60	2.851	0.969
	360	2.934	0.936
LC4M50	7	2.795	0.958
	60	2.896	0.978
	360	2.952	0.962
LC4M300	7	2.718	0.956
	60	2.876	0.983
	360	2.967	0.978
LC8M50	7	2.839	0.956
	60	2.916	0.983
	360	2.969	0.979
LC8M300	7	2.709	0.958
	60	2.885	0.968
	360	2.987	0.976

Table 5 shows that D_s values of all LHP concrete are between 2.709 and 2.987 and increase with hydration time. According to the fractal theory, D_s is meaningful between 2.0 and 3.0 for a porous material, and the material with a D_s value >3.0 or <2.0 is considered non fractal [51,97]. When the D_s value is close to 3, it means the pore structure becomes rougher and more complex [80]. Therefore, the pore structures of LHP concrete and concretes containing MgO in this study have obvious fractal characteristics.

From Table 5, it can be observed that the presence of MgO could make the pore structures of LHP concrete rougher since the D_s values of LHP concrete are increased due to MgO addition. This is a widely reported phenomenon when admixtures are used in concrete. Table 6 summarizes the D_s values determined by Zhang's model and Neimark's model in this study and other studies in recent years. Table 6 clearly illustrates that the addition of admixtures such as silica fume (SF), fly ash, and granulated blast furnace slag (GBFS), etc., could noticeably increase the D_s values, since these admixtures could make the pore structure of cement-based materials more complex [10,51,59,97].

Table 6. Fractal dimensions determined by various fractal models in this study and other literature.

Samples	Fractal Dimension Type	Fractal Dimension Value	Method	Fractal Model	Source
LHP concrete (W/B = 0.4)	D_s	2.721–2.934	MIP	Zhang's model	In this study
LHP concrete (W/B = 0.4, 4–8% MgO)	D_s	2.709–2.987	MIP	Zhang's model	In this study
OPC concrete (W/B = 0.4)	D_s	2.822–2.942	MIP	Zhang's model	[10]
LHP concrete (W/B = 0.4, 4–12% SF)	D_s	2.756–2.981	MIP	Zhang's model	[10]
Concrete (W/B = 0.5)	D_s	2.928–2.965	MIP	Zhang's model	[59]
Concrete (W/B = 0.5, 10–30% fly ash)	D_s	2.949–2.996	MIP	Zhang's model	[59]
Concrete (W/B = 0.5, 15–35% GGBS)	D_s	2.906–2.987	MIP	Zhang's model	[59]
Concrete (W/B = 0.5, 5–10% SF)	D_s	2.989–3.000	MIP	Zhang's model	[59]
Concrete	D_s	2.834–2.984	MIP	Zhang's model	[98]
Mortar (W/B = 0.3–0.5)	D_s	2.23–2.35	MIP	Zhang's model	[51]
Mortar (W/B = 0.3–0.5, 70% GGBS)	D_s	2.77–2.89	MIP	Zhang's model	[51]
Pastes	D_s	2.487–2.695	MIP	Zhang's model	[97]
Pastes added fly ash	D_s	2.454–2.782	MIP	Zhang's model	[97]
Pastes	D_s	2.592–2.965	MIP	Neimark's model	[97]
Pastes added fly ash	D_s	2.620–2.997	MIP	Neimark's model	[97]

3.7. Pore Structural and Fractal Analysis of Shrinkage Behavior

3.7.1. Correlation between Pore Structure and D_s

Figure 5 reveals the correlation between pore structure of concrete and D_s. The relationship between D_s and the porosity can be seen in Figure 5a. Many researchers confirmed that the fine pores less than 50 nm dominantly affect the shrinkage behavior of concrete [36,61,99–104]. The $V_{2.5–50\ nm}$ values estimated from Table 4 are shown in Table 7. The relationship between D_s and $V_{2.5–50\ nm}$ is displayed in Figure 5b.

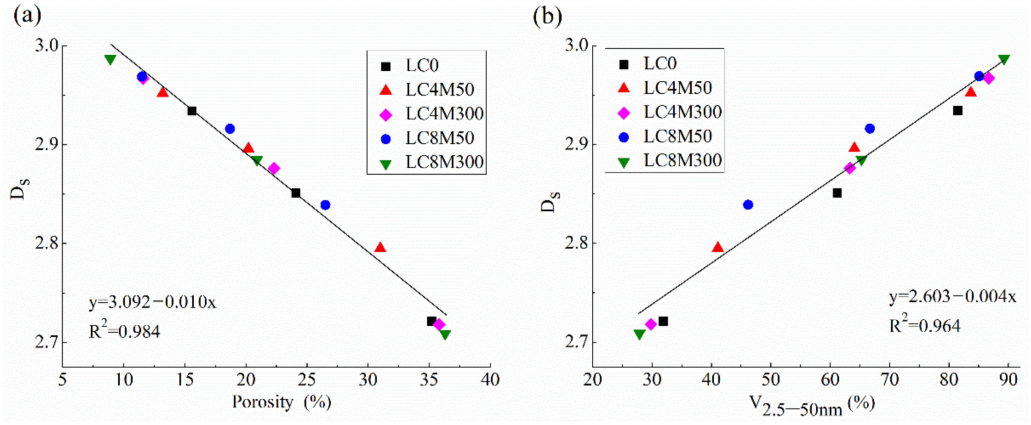

Figure 5. Relationship between D_s and (**a**) porosity and (**b**) $V_{2.5–50\ nm}$ of concrete.

Table 7. $V_{2.5–50\ nm}$ of LHP concrete added with MgO.

Notation	Hydration Time (Days)	$V_{2.5–50\ nm}$ (%)
LC0	7	31.9
	60	61.2
	360	81.5
LC4M50	7	41.1
	60	64.1
	360	83.7
LC4M300	7	29.8
	60	63.3
	360	86.7
LC8M50	7	46.2
	60	66.7
	360	85.1
LC8M300	7	27.9
	60	65.3
	360	89.3

Figure 5a indicates that D_s is negatively correlated with the porosity of LHP concrete with a high R^2 value of 0.98. This trend is in good agreement with previous findings [51–53,55,59,98]. Additionally, Figure 5b indicates that D_s exhibits a negatively linear correlation with $V_{2.5–50\ nm}$, and the R^2 between them is 0.964. The results indicate that the pore structure of LHP concrete can be studied by D_s. As Jin et al. [59] stated, D_s can perform more accurately and comprehensively than other pore structure parameters to characterize the overall situations of pore structures.

3.7.2. Pore Structural and Fractal Study on Shrinkage Behavior

The correlation between autogenous shrinkage and pore structure (porosity and $V_{2.5–50\ nm}$) was plotted in Figure 6. The correlation between drying shrinkage and pore structure is shown in Figure 7.

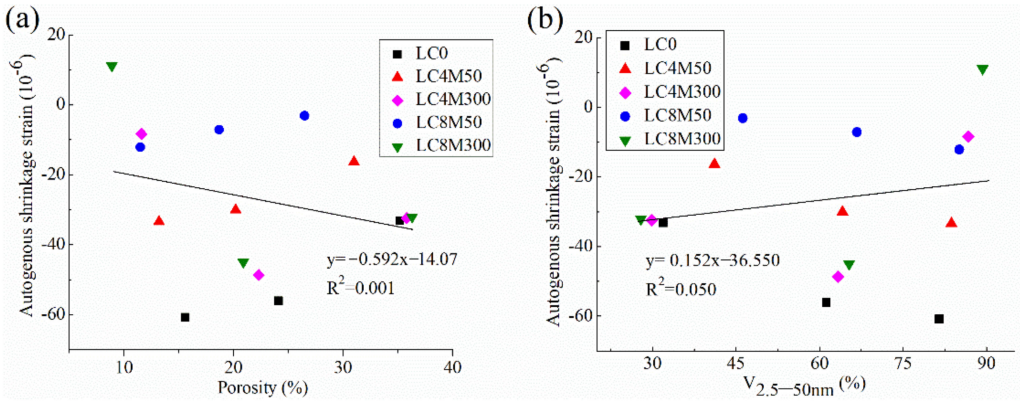

Figure 6. Correlation of autogenous shrinkage with (**a**) porosity and (**b**) $V_{2.5–50\ nm}$.

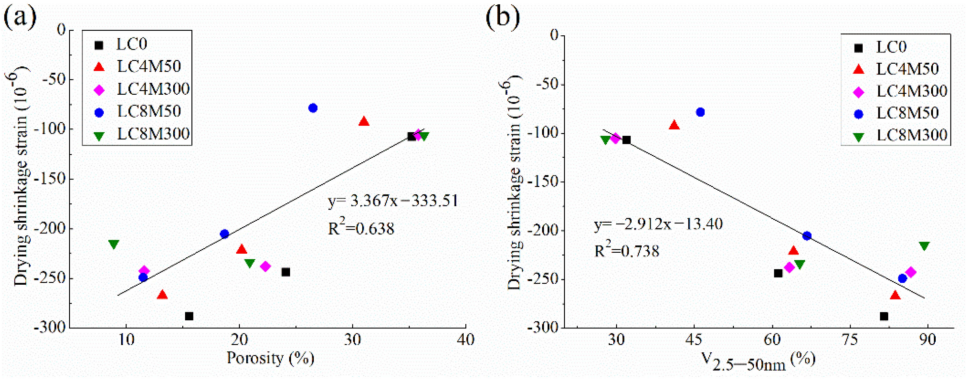

Figure 7. Correlation of drying shrinkage with (**a**) porosity and (**b**) $V_{2.5–50\ nm}$.

Figures 6 and 7 indicate that there are weak or no correlations between shrinkage behavior and pore structure parameters of LHP concrete added with MgO, since the data are scattered in these figures and R^2 values between them are not very high; some of them are even less than 0.1. This means the shrinkage behavior of these concretes are not closely related with their pore structures. However, this finding seems contradictory to the common consensus that the pores have a dominate role in determining the shrinkage of concrete. For instance, Li et al. [99] reported that the pores with a size range of 5–50 nm largely affect the shrinkage because the capillary stress is easy to develop within the pores in this size range. Wang et al. [5,10] revealed the shrinkage of concrete is linearly correlated with its porosity and $V_{2.5–50\ nm}$. This seemingly conflicting results may be explained by the following points: the shrinkage of concrete incorporated with MgO is not solely influenced by the pores, but also critically affected by the expansion of concrete which depends on the MgO dosage and reactivity. Specifically, the hydration products of MgO could fill into the large pore and increase the proportions of fine pores, as evidenced in Section 3.5. Moreover, such hydration products in solid phase (i.e., not in pores) could cause expansion in concrete and thus directly reducing or completely compensating the shrinkage of concrete, as revealed in Sections 3.3 and 3.4. Therefore, no close and definite correlation between shrinkage behavior of expansive concretes and their pore structure parameters can be found in this study.

Figure 8 shows the correlation of concrete shrinkage in this study with D_s, which are helpful for the understanding of shrinkage behavior from the standpoint of fractal theory.

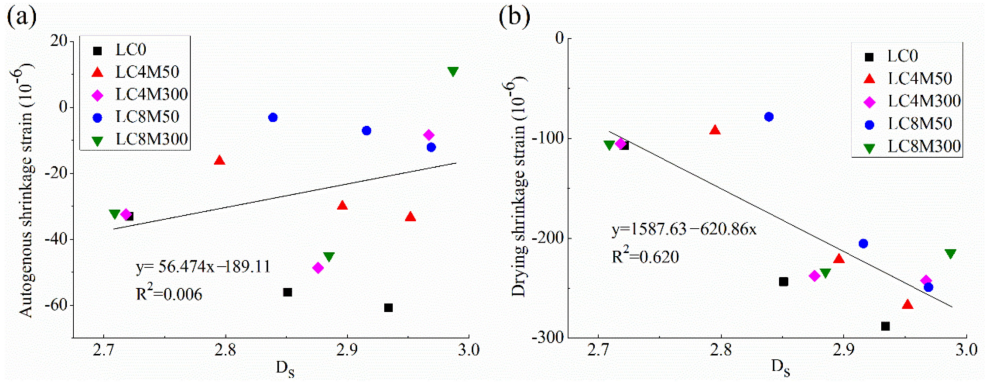

Figure 8. Correlation of D_s with (**a**) autogenous shrinkage and (**b**) drying shrinkage.

Figure 8 indicates that there is no close relationship between shrinkage strains of LHP concrete added with MgO and D_s because the R^2 values between them are low. This can be expected because pore structure parameters of expansive concrete in this study are closely correlated with D_s whereas they exhibit weak or no correlations with shrinkage behavior, as revealed above. As a result, D_s which characterizes the overall pore structures exhibits a poor relationship with shrinkage strains of LHP concrete containing MgO.

4. Conclusions

The following conclusions are obtained.

(1) The addition of reactive MgO (M50) not only extends the induction stage of LHP cement by about 1–2 h, but also increases the hydration heat, and these effects enhance with the increase in M50 dosage from 4% to 8%. In contrast, the addition of weak reactive MgO (M300) could not prolong the induction stage of LHP cement, but reduce slightly the maximal heat flow and hydration heat.

(2) The addition of M50 and M300 within the dosage range of 4–8% lowers the mechanical property of LHP concrete by 6.5–16.9 %, 5.9–16.0 %, and 0.4–16.8 % at 3, 28, and 360 days, respectively. Higher content and stronger reactivity of MgO lead to larger reductions in strength at all hydration ages. The addition of M300 favors the long-term strength increment of LHP concrete, whereas M50 is not helpful for the strength development at late age.

(3) M50 can effectively compensate the shrinkage of LHP concrete during the first few weeks, but this compensation effect disappears afterwards. In contrast, M300 starts to reduce the shrinkage at around 50–90 days and compensates for the long-term shrinkage more effectively than M50. Increasing MgO dosage could enhance the compensation effect of MgO. M300 with a dosage of 8 wt.% is suggested to be adopted in mass LHP concrete structures, but the strength loss should be considered.

(4) The addition of M50 obviously refines the pore structures of LHP concrete at 7 days, whereas M300 starts to refine the pore structure at around 60 days. At 360 days, the concretes containing M300 exhibit much finer pore structure than those containing M50 and the control LHP concrete. The pore structures improve with MgO content up to 8 wt.%.

(5) D_s of LHP concrete exhibits a close correlation with the main pore structure parameters. Both the pore structure parameters and D_s exhibit weak (or no) correlations with shrinkage behavior value. This is because the shrinkage behavior of LHP concrete incorporated with MgO is not only influenced by the pores, but also critically affected by the expansion of concrete caused by MgO.

Author Contributions: Conceptualization, writing—original draft, writing—review and editing, investigation, formal analysis, supervision, project administration funding acquisition, L.W.; investigation, X.L., L.L. (Lisheng Liu), J.X., G.Z., F.G. and L.L. (Li Li). All authors have read and agreed to the published version of the manuscript.

Funding: The authors appreciate the financial support provided by the Opening Funds of the Belt and Road Special Foundation of the State Key Laboratory of Hydrology-Water Resources and Hydraulic Engineering (2020492311), Opening Funds of the State Key Laboratory of Building Safety and Built Environment and the National Engineering Research Center of Building Technology (BSBE2020-2), the Opening Project of the State Key Laboratory of Green Building Materials (2020GBM07), the Natural Science Research Project of the Shaanxi Provincial Department of Education (20JK0722), and the National Natural Science Foundation of China (51409016 and 51808133).

Institutional Review Board Statement: Studies not involving humans.

Informed Consent Statement: Studies not involving humans.

Data Availability Statement: The data that support the findings of this study are available from the corresponding author upon reasonable request.

Acknowledgments: The authors would like to thank all the anonymous referees for their constructive comments and suggestions.

Conflicts of Interest: The authors declare no conflict of interest.

References

1. Mori, K.; Fukunaga, T.; Sugiyama, M.; Iwase, K.; Oishi, K.; Yamamuro, O. Hydration properties and compressive strength development of low heat cement. *J. Phys. Chem. Solids* **2012**, *73*, 1274–1277. [CrossRef]
2. Koumpouri, D.; Angelopoulos, G.N. Effect of boron waste and boric acid addition on the production of low energy belite cement. *Cem. Concr. Compos.* **2016**, *68*, 1–8. [CrossRef]
3. Wang, L.; Dong, Y.; Zhou, S.H.; Chen, E.; Tang, S.W. Energy saving benefit, mechanical performance, volume stabilities, hydration properties and products of low heat cement-based materials. *Energ. Build.* **2018**, *170*, 157–169. [CrossRef]
4. Maheswaran, S.; Kalaiselvam, S.; Saravana Karthikeyan, S.K.S.; Kokila, C.; Palani, G.S. β-Belite cements (β-dicalcium silicate) obtained from calcined lime sludge and silica fume. *Cem. Concr. Compos.* **2016**, *66*, 57–65. [CrossRef]
5. Wang, L.; Yang, H.Q.; Dong, Y.; Chen, E.; Tang, S.W. Environmental evaluation, hydration, pore structure, volume deformation and abrasion resistance of low heat Portland (LHP) cement-based materials. *J. Clean. Prod.* **2018**, *203*, 540–558. [CrossRef]
6. Wang, L.; Yang, H.Q.; Zhou, S.H.; Chen, E.; Tang, S.W. Mechanical properties, long-term hydration heat, shinkage behavior and crack resistance of dam concrete designed with low heat Portland (LHP) cement and fly ash. *Constr. Build. Mater.* **2018**, *187*, 1073–1091. [CrossRef]
7. Wang, L.; Yang, H.Q.; Zhou, S.H.; Chen, E.; Tang, S.W. Hydration, mechanical property and C-S-H structure of early-strength low-heat cement-based materials. *Mater. Lett.* **2018**, *217*, 151–154. [CrossRef]
8. Klemczak, B.; Batog, M.; Pilch, M.; Żmij, A. Analysis of cracking risk in early age mass concrete with different aggregate types. *Procedia Eng.* **2017**, *193*, 234–241. [CrossRef]
9. Xie, Z.; Zhu, Z.; Fu, Z.; Lv, X. Simulation of the temperature field for massive concrete structures using an interval finite element method. *Eng. Comput.* **2020**, *37*, 45. [CrossRef]
10. Wang, L.; Jin, M.M.; Wu, Y.H.; Zhou, Y.X.; Tang, S.W. Hydration, shrinkage, pore structure and fractal dimension of silica fume modified low heat Portland cement-based materials. *Constr. Build. Mater.* **2021**, *272*, 121952. [CrossRef]
11. Ha, J.H.; Jung, Y.S.; Cho, Y.G. Thermal crack control in mass concrete structure using an automated curing system. *Automat. Constr.* **2014**, *45*, 16–24. [CrossRef]
12. Wang, L.; Guo, F.X.; Lin, Y.Q.; Yang, H.M.; Tang, S.W. Comparison between the effects of phosphorous slag and fly ash on the C-S-H structure, long-term hydration heat and volume deformation of cement-based materials. *Constr. Build. Mater.* **2020**, *250*, 118807. [CrossRef]
13. Wang, L.; Guo, F.X.; Yang, H.M.; Wang, Y.; Tang, S.W. Comparison of fly ash, PVA fiber, MgO and shrinkage-reducing admixture on the frost resistance of face slab concrete via pore structural and fractal analysis. *Fractals* **2021**, *29*, 2140002. [CrossRef]
14. Zhang, P.; Wang, K.X.; Wang, J.; Guo, J.J.; Ling, Y.F. Macroscopic and microscopic analyses on mechanical performance of metakaolin/fly ash based geopolymer mortar. *J. Clean. Prod.* **2021**, *294*, 126193. [CrossRef]
15. Dong, Y.; Yang, H.; Rao, M. Effects of mineral admixture on the carbonic acid leaching resistance of cement-based materials. *Ceram. Silik.* **2017**, *61*, 276–284. [CrossRef]
16. Prasad, N.; Murali, G.; Abid, S.R.; Vatin, N.; Fediuk, R.; Amran, M. Effect of needle Type, number of layers on FPAFC composite against low-velocity projectile impact. *Buildings* **2021**, *11*, 668. [CrossRef]
17. Zhang, P.; Gao, Z.; Wang, J.; Wang, K. Numerical modeling of rebar-matrix bond behaviors of nano-SiO_2 and PVA fiber reinforced geopolymer composites. *Ceram. Int.* **2021**, *47*, 11727–11737. [CrossRef]
18. Wang, L.; Zhou, S.H.; Shi, Y.; Tang, S.W.; Chen, E. Effect of silica fume and PVA fiber on the abrasion resistance and volume stability of concrete. *Compos. Part B Eng.* **2017**, *130*, 28–37. [CrossRef]
19. Ramkumar, V.; Murali, G.; Asrani, N.P.; Karthikeyan, K. Development of a novel low carbon cementitious two stage layered fibrous concrete with superior impact strength. *J. Build. Eng.* **2019**, *25*, 100841. [CrossRef]
20. Wang, X.; Wu, D.; Zhang, J.; Yu, R.; Hou, D.; Shui, Z. Design of sustainable ultra-high performance concrete: A review. *Constr. Build. Mater.* **2021**, *307*, 124643. [CrossRef]
21. Zhang, P.; Wang, K.X.; Wang, J.; Guo, J.J.; Hu, S.W.; Ling, Y.F. Mechanical properties and prediction of fracture parameters of geopolymer/alkali-activated mortar modified with PVA fiber and nano-SiO_2. *Ceram. Int.* **2020**, *46*, 20027–20037. [CrossRef]
22. Prasad, N.; Murali, G. Research on flexure and impact performance of functionally-graded two-stage fibrous concrete beams of different sizes. *Constr. Build. Mater.* **2021**, *288*, 123138. [CrossRef]
23. Yuan, B.; Li, Z.; Chen, Y.; Hong, N.; Zhao, Z.; Chen, W.; Zhao, J. Mechanical and microstructural properties of recycling granite residual soil reinforced with glass fiber and liquid-modified polyvinyl alcohol polymer. *Chemosphere* **2021**, *268*, 131652. [CrossRef] [PubMed]
24. Yang, Z.Y.; He, J.R.; Luo, G.Q. Crack prevention techniques for face concrete of Hongjiadu CFRD with height about 200 m. *Water Power* **2008**, *7*, 59–63.
25. Mo, L.W.; Fang, J.W.; Hou, W.H.; Ji, X.K. Synergetic effects of curing temperature and hydration reactivity of MgO expansive agents on their hydration and expansion behaviours in cement pastes. *Constr. Build. Mater.* **2019**, *207*, 206–217. [CrossRef]
26. Gao, P.W.; Wu, S.X.; Lin, P.H.; Wu, Z.R.; Tang, M.S. The characteristics of air void and frost resistance of RCC with fly ash and expansive agent. *Constr. Build. Mater.* **2006**, *20*, 586–590. [CrossRef]
27. Chen, X.; Yang, H.Q.; Li, W.W. Factors analysis on autogenous volume deformation of MgO concrete and early thermal cracking evaluation. *Constr. Build. Mater.* **2016**, *118*, 276–285. [CrossRef]

28. Kabir, H.; Hooton, R.D. Evaluating soundness of concrete containing shrinkage-compensating MgO admixtures. *Constr. Build. Mater.* **2020**, *253*, 119141. [CrossRef]
29. Chen, X.; Yang, H.Q.; Zhou, S.H.; Li, W.W. Sensitive evaluation on early cracking tendency of concrete with inclusion of light-burnt MgO. *J. Wuhan Univ. Technol. Mater. Sci. Ed.* **2011**, *26*, 1018–1022. [CrossRef]
30. Ruan, S.; Unluer, C. Comparison of the environmental impacts of reactive magnesia and calcined dolomite and their performance under different curing conditions. *J Mater. Civ. Eng.* **2018**, *30*, 04018279. [CrossRef]
31. Huang, K.J.; Shi, X.J.; Dan, Z.; Mirsayar, M.; Wang, A.G.; Mo, L.W. Use of MgO expansion agent to compensate concrete shrinkage in jointed reinforced concrete pavement under high-altitude environmental conditions. *Constr. Build. Mater.* **2019**, *202*, 528–536. [CrossRef]
32. *DL/T 5296-2013. Technical Specification of Magnesium Oxide Expansive for Use in Hydraulic Concrete, China*; China Electric Power Press: Beijing, China, 2014.
33. Cao, F.Z.; Yan, P.Y. The influence of the hydration procedure of MgO expansive agent on the expansive behavior of shrinkage-compensating mortar. *Constr. Build. Mater.* **2019**, *202*, 162–168. [CrossRef]
34. Cao, F.Z.; Miao, M.; Yan, P.Y. Effects of reactivity of MgO expansive agent on its performance in cement-based materials and an improvement of the evaluating method of MEA reactivity. *Constr. Build. Mater.* **2018**, *187*, 257–266. [CrossRef]
35. Liu, P.; Chen, Z.Y.; Deng, M. Regulating the expansion characteristics of cementitious materials using blended MgO-type expansive agent. *Materials* **2019**, *12*, 976. [CrossRef] [PubMed]
36. Wang, L.; Li, G.; Li, X.; Guo, F.; Tang, S.; Lu, X.; Hanif, A. Influence of reactivity and dosage of MgO expansive agent on shrinkage and crack resistance of face slab concrete. *Cem. Conc. Compos.* **2022**, *126*, 104333. [CrossRef]
37. *CBMF 19-2017. Magnesium Oxide Expansive Agent for Concrete*; China Building Materials Industry Press: Beijing, China, 2017.
38. *ASTMC150/C150M-2016. Standard Specification for Portland Cement*; ASTM International: West Conshohocken, PA, USA, 2016.
39. *200-2003, G.Standard Specification for Moderate Heat Silicate Cement, Low Heat Portland Cement, Slag Added-Low Heat Portland Cement, China*; China Standard Press: Beijing, China, 2003.
40. *ASTM C1702-17. Standard Test Method for Measurement of Heat of Hydration of Hydraulic Cementitious Materials Using Isothermal Conduction Calorimetry*; ASTM International: West Conshohocken, PA, USA, 2009.
41. Niu, M.; Zhang, J.; Li, G. Mechanical properties of polyvinyl alcohol fiber-reinforced sulfoaluminate cement mortar containing high-volume of fly ash. *J. Build. Eng.* **2021**, *35*, 101988. [CrossRef]
42. Tang, S.W.; Li, Z.J.; Chen, E.; Shao, H.Y. Impedance measurement to characterize the pore structure in portland cement paste. *Constr. Build. Mater.* **2014**, *51*, 106–112. [CrossRef]
43. Niu, M.; Li, G.; Li, Q.; Zhang, G. Influence of naphthalene sulphonated and polycarboxylate acid-based superplasticizer on the mechanical properties and hydration behavior of ternary binder: A comparative study. *Constr. Build. Mater.* **2021**, *312*, 125374. [CrossRef]
44. Tang, S.W.; Li, Z.J.; Zhu, H.G.; Shao, H.Y.; Chen, E. Permeability interpretation for young cement paste based on impedance measurement. *Constr. Build. Mater.* **2014**, *59*, 120–128. [CrossRef]
45. *DL/T 5150-2017. Test Code for Hydraulic Concrete, China*; China Electric Power Press: Beijing, China, 2017.
46. Deboodt, T.; Fu, T.; Ideker, J.H. Evaluation of FLWA and SRAs on autogenous deformation and long-term drying shrinkage of high performance concrete. *Constr. Build. Mater.* **2016**, *119*, 53–60. [CrossRef]
47. Wongkeo, W.; Thongsanitgarn, P.; Chaipanich, A. Compressive strength and drying shrinkage of fly ash-bottom ash-silica fume multi-blended cement mortars. *Mater. Des.* **2012**, *36*, 655–662. [CrossRef]
48. Lv, X.D.; Shen, W.G.; Dong, Y.; Zhang, J.F.; Xie, Z.Q. A comparative study on the practical utilization of iron tailings as a complete replacement of normal aggregates in dam concrete with different gradation. *J. Clean. Prod.* **2019**, *211*, 704–715. [CrossRef]
49. Hu, X.; Shi, C.J.; Shi, Z.G.; Tong, B.H.; Wang, D.H. Early age shrinkage and heat of hydration of cement-fly ash-slag ternary blends. *Constr. Build. Mater.* **2017**, *153*, 857–865. [CrossRef]
50. Wang, L.; He, T.S.; Zhou, Y.X.; Tang, S.W.; Tan, J.J.; Liua, Z.T.; Su, J.W. The influence of fiber type and length on the cracking resistance, durability and pore structure of face slab concrete. *Constr. Build. Mater.* **2021**, *282*, 122706. [CrossRef]
51. Zeng, Q.; Luo, M.Y.; Pang, X.Y.; Li, L.; Li, K.F. Surface fractal dimension: An indicator to characterize the microstructure of cement-based porous materials. *Appl. Surf. Sci.* **2013**, *282*, 302–307. [CrossRef]
52. Wang, L.; Jin, M.M.; Guo, F.X.; Wang, Y.; Tang, S.W. Pore structural and fractal analysis of the influence of fly ash and silica fume on the mechanical property and abrasion resistance of concrete. *Fractals* **2021**, *29*, 2140003. [CrossRef]
53. Wang, L.; Luo, R.Y.; Zhang, W.; Jin, M.M.; Tang, S.W. Effects of fineness and content of phosphorus slag on cement hydration, permeability, pore structure and fractal dimension of concrete. *Fractals* **2021**, *29*, 2140004. [CrossRef]
54. Wang, L.; Chen, E.; Ruan, S.; Tang, S. Editorial: New technologies for investigating microstructures and enhancing performance of cementitious materials. *Front. Mater.* **2021**, *8*, 669862. [CrossRef]
55. Wang, L.; Tang, S.W. Editorial: An introduction to fractals in construction materials. *Fractals* **2021**, *29*, 2102001. [CrossRef]
56. Neimark, A.V. A new approach to the determination of the surface fractal dimension of porous solids. *Phys. A* **1992**, *191*, 258–262. [CrossRef]
57. Tang, S.W.; Cai, R.J.; He, Z.; Cai, X.H.; Shao, H.Y.; Li, Z.J.; Yang, H.M.; Chen, E. Continuous microstructural correlation of slag/superplasticizer cement pastes by heat and impedance methods via fractal analysis. *Fractals* **2017**, *25*, 1740003. [CrossRef]

58. Tang, S.W.; Huang, J.S.; Duan, L.; Yu, P.; Chen, E. A review on fractal footprint of cement-based materials. *Powder Technol.* **2020**, *370*, 237–250. [CrossRef]
59. Jin, S.S.; Zhang, J.X.; Han, S. Fractal analysis of relation between strength and pore structure of hardened mortar. *Constr. Build. Mater.* **2017**, *135*, 1–7. [CrossRef]
60. Tang, S.W.; He, Z.; Cai, X.H.; Cai, R.J.; Zhou, W.; Li, Z.J.; Shao, H.Y.; Wu, T.; Chen, E. Volume and surface fractal dimensions of pore structure by NAD and LT-DSC in calcium sulfoaluminate cement pastes. *Constr. Build. Mater.* **2017**, *143*, 395–418. [CrossRef]
61. Wang, L.; Zeng, X.; Yang, H.; Lv, X. Investigation and application of fractal theory in cement-based materials: A review. *Fractal Fract.* **2021**, *5*, 247. [CrossRef]
62. Tang, S.W.; Chen, E.; Shao, H.Y.; Li, Z.J. A fractal approach to determine thermal conductivity in cement pastes. *Constr. Build. Mater.* **2015**, *74*, 73–82. [CrossRef]
63. Tang, S.W.; Yuan, J.H.; Cai, R.J.; Chen, E. In situ monitoring of hydration of magnesium oxysulfate cement paste: Effect of $MgO/MgSO_4$ ratio. *Constr. Build. Mater.* **2020**, *251*, 119003–119013. [CrossRef]
64. Shi, Y.; Dong, Y.; Chen, X.; Li, X. Different chemical composition of aggregate impact on hydraulic concrete interfacial transition zone. *Asian J. Chem.* **2014**, *26*, 1267–1270. [CrossRef]
65. Tang, S.W.; Wang, L.; Cai, R.J.; Cai, X.H.; He, Z.; Chen, E. The evaluation of electrical impedance of three-dimensional fractal networks embedded in a cube. *Fractals* **2017**, *25*, 1740005. [CrossRef]
66. Tang, S.W.; Cai, X.H.; Zhou, W.; Shao, H.Y.; He, Z.; Li, Z.J.; Ji, W.M.; Chen, E. In-situ and continuous monitoring of pore evolution of calcium sulfoaluminate cement at early age by electrical impedance measurement. *Constr. Build. Mater.* **2016**, *117*, 8–19. [CrossRef]
67. Mandelbrot, B.B. The fractal geometry of nature. *Am. J. Phys.* **1988**, *51*, 468. [CrossRef]
68. Tang, S.W.; Wang, Y.; Geng, Z.C.; Xu, X.F.; Yu, W.Z. Structure, fractality, mechanics and durability of calcium silicate hydrates. *Fractal Fract.* **2021**, *5*, 47. [CrossRef]
69. Mandelbrot, B.B. *The Fractal Geometry of Nature*; W.H. Freeman and Company: San Francisco, CA, USA, 1983.
70. Tang, S.W.; Chen, E.; Li, Z.J.; Shao, H.Y. Assessment of steady state diffusion of volatile organic compounds in unsaturated building materials based on fractal diffusion model. *Build. Environ.* **2015**, *84*, 221–227. [CrossRef]
71. Xiao, J.; Long, X.; Li, L.; Jiang, H.; Zhang, Y.; Qu, W. Study on the influence of three factors on mass loss and surface fractal dimension of concrete in sulfuric acid environments. *Fractal Fract.* **2021**, *5*, 146. [CrossRef]
72. Zarnaghi, V.N.; Fouroghi-Asl, A.; Nourani, V.; Ma, H. On the pore structures of lightweight self-compacting concrete containing silica fume. *Constr. Build. Mater.* **2018**, *193*, 557–564. [CrossRef]
73. Xiao, J.; Long, X.; Qu, W.; Li, L.; Jiang, H.; Zhong, Z. Influence of sulfuric acid corrosion on concrete stress-strain relationship under uniaxial compression. *Measurement* **2021**, *185*, 110318. [CrossRef]
74. Huang, J.; Li, W.; Huang, D.; Chen, E. Fractal analysis on pore structure and hydration of magnesium oxysulfate cements by first principle, thermodynamic and microstructure-based methods. *Fractal Fract.* **2021**, *5*, 164. [CrossRef]
75. Li, L.; Li, Z.L.; Cao, M.L.; Tang, Y.; Zhang, Z. Nanoindentation and porosity fractal dimension of calcium carbonate whisker reinforced cement paste after elevated temperatures (up to 900 °C). *Fractals* **2021**, *29*, 2140001. [CrossRef]
76. Xiao, J.; Qu, W.J.; Jiang, H.B.; Li, L.; Huang, J.; Chen, L. Fractal characterization and mechanical behavior of pile-soil interface subjected to sulfuric acid. *Fractals* **2021**, *29*, 2140010. [CrossRef]
77. Li, L.; Sun, H.; Zhang, Y.; Yu, B. Surface cracking and fractal characteristics of bending fractured polypropylene fiber-reinforced geopolymer mortar. *Fractal Fract.* **2021**, *5*, 142. [CrossRef]
78. Xiao, J.; Xu, Z.; Murong, Y.; Lei, B.; Chu, L.; Jiang, H.; Qu, W. Effect of chemical composition of fine aggregate on the frictional behavior of concrete–soil interface under sulfuric acid environment. *Fractal Fract.* **2022**, *6*, 22. [CrossRef]
79. Zhang, B.Q.; Liu, W.; Liu, X. Scale-dependent nature of the surface fractal dimension for bi- and multi-disperse porous solids by mercury porosimetry. *Appl. Surf. Sci.* **2006**, *253*, 1349–1355. [CrossRef]
80. Zhang, B.Q.; Li, S.F. Determination of the surface fractal dimension for porous media by mercury porosimetry. *Ind. Eng. Chem. Res.* **1995**, *34*, 1383–1386. [CrossRef]
81. Pfeifer, P.; Avnir, D. Chemistry in noninteger dimensions between two and three. I. Fractal theory of heterogeneous surfaces. *J. Chem. Phys.* **1983**, *79*, 3558–3565. [CrossRef]
82. Zheng, L.; Xuehua, C.; Mingshu, T. Hydration and setting time of MgO-type expansive cement. *Cem. Concr. Res.* **1992**, *22*, 1–5. [CrossRef]
83. Huang, L.M.; Yang, Z.H.; Wang, S.F. Influence of calcination temperature on the structure and hydration of MgO. *Constr. Build. Mater.* **2020**, *262*, 120776. [CrossRef]
84. Kuenzel, C.; Zhang, F.; Ferrandiz-Mas, V.; Cheeseman, C.R.; Gartner, E.M. The mechanism of hydration of MgO-hydromagnesite blends. *Cem. Concr. Res.* **2018**, *103*, 123–129. [CrossRef]
85. Mo, L.W.; Deng, M.; Tang, M.S. Effects of calcination condition on expansion property of MgO-type expansive agent used in cement-based materials. *Cem. Concr. Res.* **2010**, *40*, 437–446. [CrossRef]
86. Mo, L.W.; Fang, J.W.; Huang, B.; Wang, A.G.; Deng, M. Combined effects of biochar and MgO expansive additive on the autogenous shrinkage, internal relative humidity and compressive strength of cement pastes. *Constr. Build. Mater.* **2019**, *229*, 116877. [CrossRef]

87. Mo, L.W.; Liu, M.; Al-Tabbaa, A.; Deng, M. Deformation and mechanical properties of the expansive cements produced by inter-grinding cement clinker and MgOs with various reactivities. *Constr. Build. Mater.* **2015**, *80*, 1–8. [CrossRef]
88. Beshr, S.S.; Mohaimen, I.M.A.; Azline, M.N.N.; Azizi, S.N.; Nabilah, A.B.; Aznieta, A.A. Feasibility assessment on self-healing ability of cementitious composites with MgO. *J. Build. Eng.* **2021**, *34*, 101914. [CrossRef]
89. Gonçalves, T.; Silva, R.V.; de Brito, J.; Fernández, J.M.; Esquinas, A.R. Hydration of reactive MgO as partial cement replacement and its influence on the macroperformance of cementitious mortars. *Adv. Mater. Sci. Eng.* **2019**, *2019*, 9271507. [CrossRef]
90. Wang, L.; Jin, M.; Zhou, S.; Tang, S.W.; Lu, X. Investigation of microstructure of C-S-H and micro-mechanics of cement pastes under NH4NO3 dissolution by 29Si MAS NMR and microhardness. *Measurement* **2021**, *185*, 110019. [CrossRef]
91. Cao, F.Z.; Yan, P.Y. Effects of reactivity and dosage of magnesium oxide expansive agents on long-term volume variation of concrete. *J. Chin. Ceram. Soc.* **2018**, *46*, 1126–1132.
92. Cao, F.Z.; Miao, M.; Yan, P.Y. Hydration characteristics and expansive mechanism of MgO expansive agents. *Constr. Build. Mater.* **2018**, *183*, 234–242. [CrossRef]
93. Choi, S.W.; Jang, B.S.; Kim, J.H.; Lee, K.M. Durability characteristics of fly ash concrete containing lightly burnt MgO. *Constr. Build. Mater.* **2014**, *58*, 77–84. [CrossRef]
94. Mo, L.W.; Deng, M.; Wang, A. Effects of MgO-based expansive additive on compensating the shrinkage of cement paste under non-wet curing conditions. *Cem. Concr. Compos.* **2012**, *34*, 377–383. [CrossRef]
95. Huang, K.J.; Deng, M.; Mo, L.W.; Wang, Y.G. Early age stability of concrete pavement by using hybrid fiber together with MgO expansion agent in high altitude locality. *Constr. Build. Mater.* **2013**, *48*, 685–690. [CrossRef]
96. Mindess, S.; Young, J.F.; Darwin, D. *Concrete*; Prentice-Hall: Hoboken, NJ, USA, 2003.
97. Zeng, Q.; Li, K.F.; Teddy, F.C.; Patrick, D.L. Surface fractal analysis of pore structure of high-volume fly-ash cement pastes. *Appl. Surf. Sci.* **2010**, *257*, 762–768. [CrossRef]
98. Liu, P.; Cui, S.G.; Li, Z.H.; Xu, X.F.; Guo, C. Influence of surrounding rock temperature on mechanical property and pore structure of concrete for shotcrete use in a hot-dry environment of high-temperature geothermal tunnel. *Constr. Build. Mater.* **2019**, *207*, 329–337. [CrossRef]
99. Li, Y.; Bao, J.; Guo, Y. The relationship between autogenous shrinkage and pore structure of cement paste with mineral admixtures. *Constr. Build. Mater.* **2010**, *24*, 1855–1860. [CrossRef]
100. Ma, Y.; Ye, G. The shrinkage of alkali activated fly ash. *Cem. Concr. Res.* **2015**, *68*, 75–82. [CrossRef]
101. Zhang, W.; Hama, Y.; Na, S.H. Drying shrinkage and microstructure characteristics of mortar incorporating ground granulated blast furnace slag and shrinkage reducing admixture. *Constr. Build. Mater.* **2015**, *93*, 267–277. [CrossRef]
102. He, W.; Liu, C.; Zhang, L. Effects of sodium chloride on the mechanical properties of slag composite matrix geopolymer. *Adv. Cem. Res.* **2019**, *31*, 389–398. [CrossRef]
103. He, W.; Hao, W.; Meng, X.; Zhang, P.; Sun, X.; Shen, Y. Influence of graphite powder on the mechanical and acoustic emission characteristics of concrete. *Buildings* **2022**, *12*, 18. [CrossRef]
104. Chen, C.; Zhang, R.; Zhou, L.; Wang, Y. Influence of waste tire particles on freeze-thaw resistance and impermeability performance of waste tires/sand-based autoclaved aerated concrete composites. *Buildings* **2022**, *12*, 33. [CrossRef]